

Chapter 1. Getting the Inside Story: using computed X-ray tomography to study inclusion trails in garnet porphyroblasts

This chapter has been accepted for publication by The American Mineralogist as an electronic article. It is best viewed as an interactive Adobe Acrobat document, which can be found on the CD in appendix A of this thesis.

Huddleston-Holmes, C. R. & Ketcham, R. A. 2005. Getting the inside story: using computed X-ray tomography to study inclusion trails in garnet porphyroblasts. *American Mineralogist*, **90**, ea1-ea17.

Abstract

This study demonstrates how high-resolution X-ray computed tomography can be used to determine the geometry of curved inclusion trails in garnet porphyroblasts. For the first time, the three-dimensional geometry of these features is shown as an animation, a stereo pair, a VRML model and two-dimensional sections. The spatial resolution of the data in this study, approximately 10 μm , is high enough to resolve inclusions, and finer resolutions are possible. Comparisons of scan imagery to thin section and microprobe data demonstrate that many typical inclusion phases in garnet porphyroblasts can be clearly distinguished, including quartz, ilmenite and monazite. A sodium metatungstate solution with a density of 1.19 g/cm^3 was used for a wedge calibration during scanning, reducing artifacts to a minimum and allowing maximum image contrast. The overall conclusion of this study is that high-resolution X-ray computed tomography is a quick, non-destructive technique that is invaluable in the study of porphyroblast microstructure. The three-dimensional data generated by this technique can be compared with geometries predicted by the varying theoretical models for the formation of curved inclusion trails in garnet porphyroblasts. They can also be analyzed to determine the three-dimensional orientation of curvature axes in individual porphyroblasts, which has not been possible until now.

1 Introduction

This paper describes a technique that allows the geometry of curved inclusion trails in garnet porphyroblasts to be studied in three-dimensions. Curved inclusion trails are a common feature of porphyroblastic minerals in rocks from deformed metamorphic terrains. They have been a source of intrigue for nearly a century and have the potential to provide insights into the structural and metamorphic processes that occur during orogenesis. Johnson (1999) provides a good review of the current literature on porphyroblast inclusion trails. He points out one of the remaining obstacles to getting the most from these structures is the lingering uncertainty over how these features are formed. This debate centers on whether or not the porphyroblasts rotate relative to fixed geographical coordinates. In the rotational model the curved trails are the result of syn-growth rotation of the porphyroblast with respect to a foliation that is parallel to the plane of shear during simple shear or non-coaxial flow (e.g. Passchier et al. 1992, Rosenfeld 1970, Schoneveld 1977, Williams & Jiang 1999). The non-rotational model has the porphyroblast preserving the rotation of the matrix foliation about it during multiple foliation forming events (Aerden 1995, Bell et al. 1992b, Bell et al. 1992c, Ramsay 1962, Stallard & Hickey 2001). How inclusion trails are interpreted in micro-structural studies is largely dependant on which of these contradictory models for their formation is favored.

There have been many theoretical studies done attempting to predict the geometry of inclusion trails based on the mechanism of formation (e.g. Masuda & Mochizuki 1989, Samanta et al. 2002b, Schoneveld 1977, Stallard et al. 2002, Williams & Jiang 1999). Conversely, the number of studies of the three-dimensional geometry of inclusion trails in rocks is small. This is because of the difficulty of doing such a study. The traditional approach to studying these geometries has been to cut serial thin sections (Johnson 1993b, Johnson & Moore 1996), do universal stage studies (Powell & Treagus 1967, 1970) or do serial grinding/microprobe studies (e.g. Marschallinger 1998, Spear & Daniel 1998). These techniques are destructive, time consuming and sections can only be cut in one direction. Serial thin sections have a minimum interval of one to two millimeters, serial grinding is time consuming and universal stage studies deal with only a thin slice of rock. It can be difficult to correlate trails between sections and impossible to re-section the porphyroblast in different orientations. To be able to get a full appreciation of the geometry of inclusion trails a new technique is needed that allows these features to be studied in more detail.

Recently Ikeda et al. (2002) used high-resolution X-ray computed tomography (HRXCT) to look at the geometry of inclusion trails in garnet porphyroblasts in three-dimensions. X-ray computed tomography, or X-ray CT, is a technique that enables the internal structure of solid objects to be visualized in three-dimensions. It has found an ever increasing number of applications in the study of geological problems (Ketcham & Carlson 2001, Mees et al. 2003). Some of the tasks that HRXCT systems have been used for over the last ten years include palaeontological studies (e.g. Cifelli et al. 1996, Rowe 1996), non-destructive studies of meteorites (Tsuchiyama et al. 2002) and quantitative analysis of porphyroblast crystallization in metamorphic rocks (Carlson & Denison 1992, Denison et al. 1997).

X-ray CT was originally developed for medical imaging in the late 1960's and early 1970's (Natterer & Ritman 2002). The technique allows an image to be constructed that shows a thin slice through a three-dimensional object based on how it attenuates X-ray energy. Stacks of these slices make a three-dimensional representation of the object. This attenuation is closely related to the energy of the X-rays, and the average atomic number and density of the material that the X-rays are passing through. In medical CT systems the variation in density and composition of bones and other organs allow imaging of the human body. Similarly, variations in mineral density and composition allow the three-dimensional textures within a rock to be revealed. The resulting data can then be cut into an infinite number of sections in any given orientation, or viewed with various three-dimensional techniques. Another advantage of the technique is that the material is not destroyed in the process. Recent developments in the production of higher resolution industrial X-ray CT systems have resulted in increased spatial resolution, which coupled with the high density contrast between garnet and the minerals that typically form inclusion trails makes X-ray CT well suited to the study of the three-dimensional

morphology of these microstructures. The aim of this paper is to provide the reader with a background into this technique and a demonstration of its application. Parameters that can be controlled by the researcher are discussed from the point of view of obtaining optimal results.

1.1 An Introduction to Computed X-ray tomography

HRXCT, as applied in this study, is the evolution of the X-ray CT technique originally developed for medical imaging which is capable of imaging at spatial resolution 1-3 orders of magnitude greater than medical scanners in a wide range of materials. The resulting HRXCT technique has great potential for geological applications. The reader is referred to Ketcham and Carlson (2001) who give a thorough account of the current technology and its applications in the geological sciences. The key aspects of X-ray CT as related to this study are provided here.

X-ray CT works on the principal that the energy of X-rays will be attenuated as they pass through a sample, and that the amount of attenuation is related to certain properties of the material. The change in intensities of X-rays from before they enter the sample to after they have passed through it are measured. Beer's law relates this change in intensity between the incident intensity (I_0) and the final intensity (I) to the linear attenuation coefficient (μ):

$$I = I_0 \exp \left[- \sum_i (\mu_i x_i) \right], \quad (1)$$

where each increment i represents a single material that has an attenuation coefficient μ_i and x_i is the length of that material that the X-rays travel through.

For a single material, μ is related to the electron density of the phase (ρ), its atomic number (Z) and the energy of the X-rays (E). Figure 1 shows μ for different minerals as a function of X-ray energy. These have been calculated by multiplying mass attenuation coefficients obtained from the XCOM online database (Berger et al. 1999) by the mass density of the phase. In general, values of μ decrease as X-ray energy increases. This is a result of the increasing importance of Compton scattering at X-ray energies over 50-100kV, where the amount of attenuation is proportional to Z . Below these levels photoelectric absorption dominates, and the amount of attenuation is proportional to Z^{4-5} resulting in greater sensitivity. While lower energy X-rays provide greater sensitivity, there is a trade-off in terms of the signal-to-noise ratio and penetration with higher X-ray energies fairing better on both accounts. Typically, X-ray sources used in X-ray CT are not monochromatic and for a tungsten tube with a voltage of 160kV, the average X-ray energy will be approximately 64 kV. Equation 1 is for a single X-ray energy, and it is this equation that is solved to define μ . This is not considered a problem as the reconstructions assign a single value per pixel that represents the relative level of absorption of the X-ray energy spectra at that point. As discussed above, the ability of X-ray CT to differentiate between different minerals is dependent on several factors; however, the

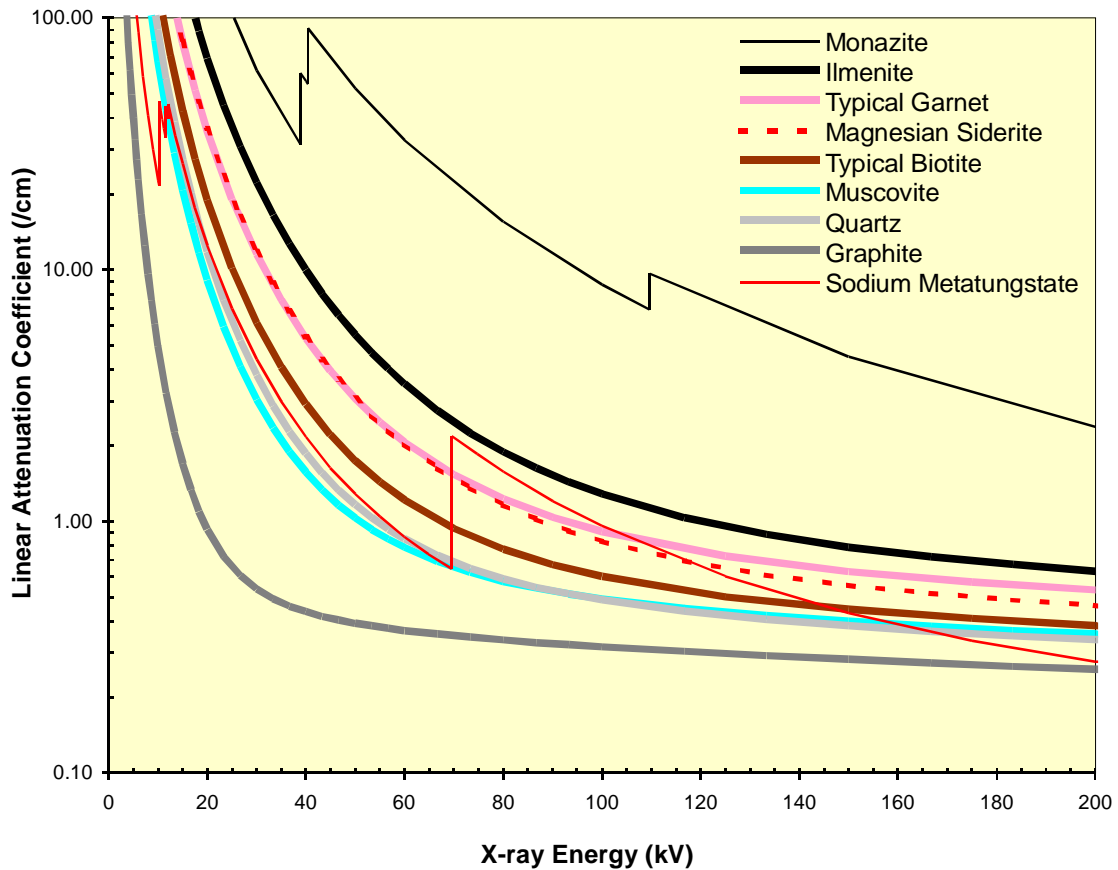


Figure 1. Linear attenuation coefficients (μ) as a function of X-ray energy for minerals typical of a garnet-bearing schist. This plot shows that garnet has a μ that is significantly higher than those matrix minerals typically found in pelitic schists, and significantly lower than those of the iron/titanium oxides. These minerals are also found as inclusions in garnet porphyroblasts and this contrast in μ values is what enables the imaging inclusion trails using X-ray CT. Note that magnesian siderite has a very similar μ to garnet, particularly at low X-ray energies. This is because the average Z-values are very similar for the two minerals. At higher X-ray energies the μ of these two minerals diverge due to the higher density of garnet. At the X-ray energies used for this study (150keV), these minerals cannot be differentiated. Muscovite and quartz show a similar trend. The spikes on the curves for sodium metatungstate (SMT) and monazite reflect the X-ray absorption edges of high-atomic-number elements. The data was generated by multiplying mass attenuation coefficients generated by the XCOM online database (Berger et al. 1999) by the mass density of the phase.

technique is sensitive enough to differentiate between minerals with as little as a 0.1% difference in attenuation coefficients (Wellington & Vinegar 1987).

The three-dimensional representations generated by X-ray CT are actually a stack of cross-sectional slices through the object of interest. Each slice is a two-dimensional image reconstructed from a series of projections or views (up to several thousand) on the same plane, with the sample being rotated relative to the source-detector pair between each view. The majority of scanning machines have what is known as a third generation geometry. This geometry consists of a fan beam X-ray source and a detector array that is wide enough to allow the whole object to fit within the fan (fig. 2b). This means that the sample only needs to rotate relative to the source-detector pair between views. The data collected in a single view is output as levels of attenuation and a profile is shown in figure 2c. Note the dome shape that is the

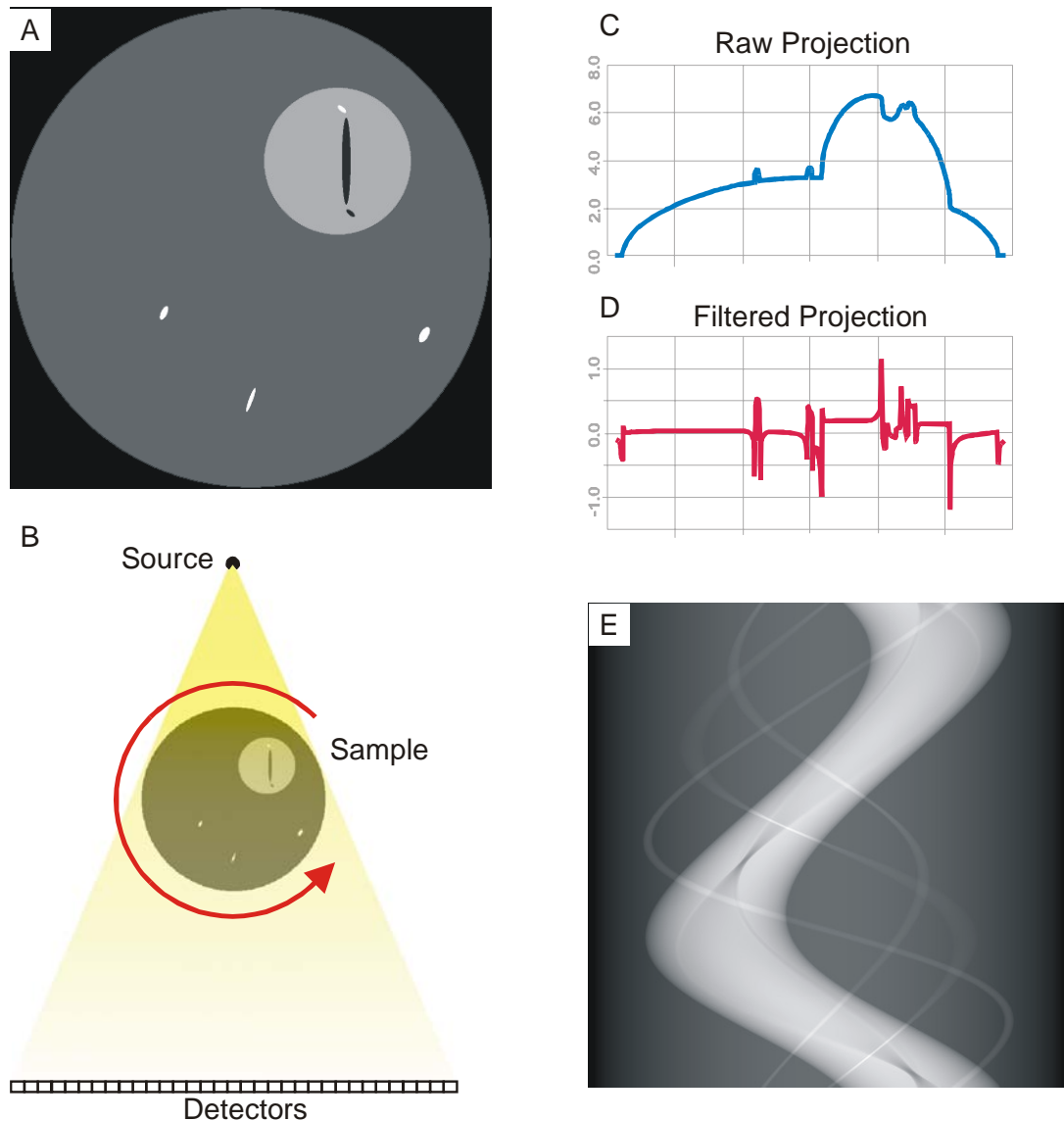


Figure 2. This figure shows how computed tomography works. A virtual phantom is shown in (A), representing a slice through a core of matrix material (dark grey), with a garnet porphyroblast (mid grey) and several iron oxide grains. The garnet has inclusions of matrix material and an iron oxide. Third generation scan geometry is shown in (B). (C) is the raw data profile for the view in (B). (D) shows the data from (B) after filtering to enhance edges before reconstruction. (E) is a sinogram of all the data from 512 detectors (columns) and 512 views (rows) for the phantom in (A). Zones of higher attenuation (garnet, iron oxides) are represented by lighter shades of grey. All of these simulations were made using CTSim (<http://www.ctsim.org>).

result of X-rays having to travel through a greater volume of rock at the center of the profile. The raw data for all views in a slice can be displayed as a sinogram (fig 2e), with each line representing the data from a single viewing angle and the columns showing values for individual detectors. Traditionally, a grey scale from dark to light is used to represent low to high attenuation levels, in keeping with conventional X-ray radiography.

The two-dimensional slice images are generated from the raw data via a mathematical process called reconstruction. There are several algorithms that can be used to reconstruct

images with a balance between computational expense, noise reduction and spatial accuracy required. The most commonly used algorithm is filtered back-projection (Kak & Slaney 1988, Natterer & Ritman 2002), in which a filter is applied to the data before the image is reconstructed. A combination between a ramp filter that accentuates contrast and reduces blurring and star patterns in the final image and a noise filter is used. This combination maintains good spatial accuracy without significantly diminishing the sensitivity of the scan. The range of filters and filter parameters provide scope for fine-tuning the image, dependent on the goals of the project and the nature of the material. Figure 2d shows the data from figure 2c after the application of a filter. The dome shape has been removed and the boundaries of the different materials have been sharpened. The final step in this process of reconstructing a tomographic image is back-projection, where the filtered data from each view is smeared across the image, as shown by the animation in figure 3. Prior to reconstruction it may be necessary to correct for drift. One way this is done is to trace the values for attenuation in air over time, equalizing them if there is a significant variation.

The resulting two-dimensional images have pixel values that correspond to the raw CT values that are scaled from low attenuation to high. This scaling has traditionally been a 12-bit range with 4096 values possible, although most modern equipment provides 16-bit (65,536 values) data. These values show the relative difference in X-ray attenuation between regions represented by each pixel. This scale is arbitrary with the key concern being to maximize the contrast between minerals in the sample. It is difficult to calibrate the system to correlate the CT values with a reference scale such as density when working with geological materials. This is because the CT values are dependent on the density and composition of the sample, the size of the sample, the energy of the X-rays and the geometry of the scan. The fact that scans are done with polychromatic X-ray sources is the biggest hindrance to a more quantitative determination of CT values. Tsuchiyama et al (2002) provide an example of the complexities in using X-ray CT for quantitative analysis of mineral compositions. This is not considered to be a necessary step for textural analysis where identification of minerals is less important or can be done by correlation with thin sections. It must be pointed out that each pixel (picture element) in a slice is more correctly a voxel (volume element), in that it has a depth equal to the thickness of the slice. The final three-dimensional volume for visualization is constructed by stacking these slices together.

The spatial resolution that can be achieved by X-ray CT is controlled by the size of the X-ray focal spot and detectors, and the ability to get satisfactory counting statistics in the measurement of the intensity of X-rays that have passed through the sample. These two factors work against each other, as a small focal spot will have lower intensity and small detectors will record fewer counts. A balance must be reached between X-ray energy, the size of the source and the detectors and of the apertures used on them, scan times and sample size. Typically, the

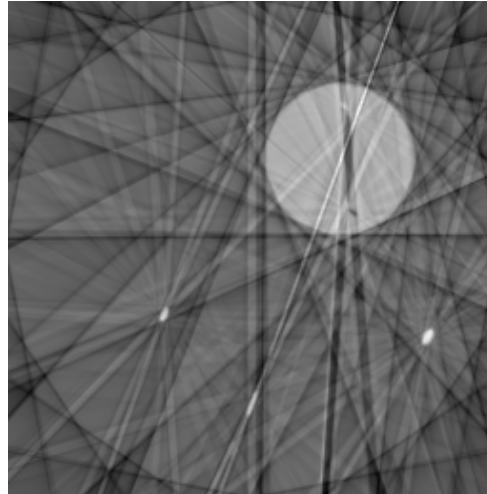


Figure 3. The animation shows the back-projection process, where the filtered data from each view is smeared over each other creating the final image. This animation was created using CTSim (<http://www.ctsim.org>) and is a reconstruction of the virtual phantom in figure 2A. The animation can be paused and stepped backward and forward one frame at a time. The frames represent 1, 2, 4, 8, 12, 16, 20, 24, 32, 48, 64, 128, 256, 512 and 1024 views respectively. The divergent nature of the material boundaries in each view is a result of the third generation scan geometry. Note the sharpness of the boundaries between the different materials, which are due to the filtering of the data before reconstruction. To view this animation, see the interactive Adobe Acrobat document on the CD in appendix A of this thesis.

two-dimensional slices are constructed as images at either a 512 x 512 or 1024 x 1024 resolution. The minimum resolution of a system therefore is one where each voxel in the reconstructed slice is of the same physical dimension as the minimum area that can be resolved when constructing the image. For modern industrial scanning systems this is roughly 3 μm for a sample 3 mm in maximum dimension. The current limitations in tube-based X-ray sources that complicate obtaining better resolution are the minimum focal spot size ($\sim 10 \mu\text{m}$ in most systems) and focal spot drift. Better resolution may be obtained with synchrotron-based CT systems, with Jones et al (2003) reporting resolutions as low as 2 μm .

Each CT voxel value represents the average attenuation within the corresponding volume of material. When that volume encompasses two or more materials of differing properties partial volume effects occur where the CT value is the volume weighted average of these different materials. In addition, because of the finite resolution of X-ray CT, voxel values are also influenced somewhat by surrounding material. These factors lead to blurring of material boundaries, and can complicate straightforward interpretation of grey level values. Conversely, this aspect of the data also allows some features that are finer than the voxel size to be detectable and even measurable. This is particularly the case for planar features such as fractures (see figure 6 of Ketcham & Carlson, 2001; Van Geet & Swennen, 2001) and high-attenuation trace phases (Kyle & Ketcham 2003). In application the minimum size of a grain that can be imaged in a rock will depend largely on the contrast in attenuation between adjacent

minerals, and the voxel size. For example, individual quartz grains in a quartzite would not be distinguishable regardless of their size whereas an ilmenite grain with dimensions close to that of a voxel may stand out from the quartz, although its attenuation signal would be smeared over several voxels. In such instances specialized calculations are required to extract reliable dimensional information. In order for a grain to be accurately measurable in a straightforward fashion, such as thresholding, as a rule it must be at least four voxels wide in each dimension.

X-ray CT scanners require offset and gain calibrations as a minimum. An additional form of calibration is a wedge calibration. In this technique a wedge of material with attenuation properties approaching those of the sample is scanned through a full rotation. This procedure provides an offset-corrected average detector reading from which all data are subtracted. Wedges are actually cylinders of material, such as garnet powder, or a solution of sodium metatungstate (SMT) in water. The advantage of an SMT solution is that it can be easily mixed to produce whatever density is desired (Krukowski 1988) it is non-toxic and as a liquid is uniform in physical properties. Because of the high attenuation coefficient of tungsten, very low concentrations can produce net attenuation coefficients similar to solid rock. The linear attenuation coefficient of a solution of SMT mixed to a density of 1.19g/cm^3 is shown on figure 1 for comparison with a range of pelitic minerals.

The two main artifacts that can occur in X-ray CT are beam hardening and ring artifacts. Beam hardening is caused by the preferential attenuation of lower energy X-rays as they pass through the object being scanned. The result is that the material closer to the source has a different X-ray spectrum passing through it than that further along the X-ray path. In the final image this results in the center of the image appearing to cause less attenuation than the edges. Star patterns and streaks emanating from highly attenuating objects in the final image are also due to beam hardening. Steps can be taken during sample preparation, scanning, data filtering and image reconstruction to remove the effects of beam hardening. The most successful is the wedge calibration that effectively removes the lower-energy X-rays from consideration. Ring artifacts are the result of anomalous responses from individual or sets of detectors. They result in circular features centered on the rotation axis in the final image. Again a variety of techniques can be employed to correct for this artifact with wedge calibration and data filtering being the most effective.

1.2 Sample Description

The oriented sample selected for this study, V209, was collected from the Cram Hill Formation in southeastern Vermont. This rock was chosen because it has a high density of garnet porphyroblasts, most with well developed inclusion trails (fig. 4) and previous work (Bell et al. 1998) has shown that two distinct foliation curvature axes are preserved from core to rim. It is a carbonaceous pelite that has been metamorphosed to amphibolite facies and contains

quartz, muscovite, garnet, biotite, calcite, ilmenite and trace epidote. Grain sizes of matrix minerals are shown in table 1. The sample is compositionally banded with mica rich and quartz rich bands at a sub-centimeter scale. The mica rich bands have a slightly higher garnet density than the quartz rich areas. Fine graphite is present throughout the rock as a fine dusting of grains that in places form density bands.

Almandine-rich garnet and biotite are present as porphyroblastic phases with the latter restricted to the quartz-rich bands in the matrix. Garnet porphyroblasts have only partially developed crystal faces and inclusion trails composed of elongate quartz, ilmenite grains, fine graphite, magnesian siderite and bands of hydrated Fe-oxide with pyrophyllite and quartz. The hydrated Fe-oxide/clay bands are the result of alteration along inclusion rich bands that probably represented some form of compositional layering in the rock prior to garnet growth. The composition of these precursor inclusions cannot be determined. The orientation of these bands does not appear to have been changed by the alteration process. Inclusion trail density is higher in porphyroblasts that are in the quartz rich bands. The grain sizes of the inclusions are given in table 1. A texturally distinct core and rim is preserved within the garnet porphyroblasts with the latter having few inclusions other than graphite. The core-rim transition is coincident with a drop in Ca content seen in X-ray compositional maps (fig. 5) that also show weak compositional zoning. Iron stained micro-fractures in garnet porphyroblasts are visible in the photomicrographs. Some biotite porphyroblasts have inclusion trails defined by graphitic bands and rare elongate quartz grains.

Phase	Matrix (mm)	Inclusions (mm)
Garnet*	1.0 – 4.0	not applicable
Biotite*	0.2 – 0.6	not applicable
Quartz	0.060 – 0.150	< 0.100
Micas	<0.015	not present
Ilmenite	0.1 – 0.25	0.1 – 0.25
Magnesian Siderite	not present	< 0.050
Graphite	< 0.004	< 0.004

* Porphyroblastic phases.

Table 1. Grain sizes of porphyroblastic, matrix and inclusion phases. Many of the grains are elongate and the long axis dimensions only are given here. Where a definite minimum grain size is observed a range is given. Matrix quartz has two distinct domains with quartz in mica rich areas having a maximum grain size of 0.080 mm.

2 Methodology

2.1 Sample preparation

Sample preparation for X-ray CT began with cutting a 30mm thick, horizontal slab from the specimen. Samples were then prepared by drilling a vertical core 11mm in diameter through the slab. In order to preserve the orientation information, a north-south groove was made in the top surface of the specimen before coring, and a piece of wire with a notch at the northern end was glued into the groove after coring. This provided an orientation marker that could be clearly imaged by X-ray CT. A core is used because a cylinder is the ideal shape for X-ray CT analysis as it images a circular field of view. No other sample preparation was necessary.

2.2 Computed X-ray tomography

The scanner used for this study is at the University of Texas (UT) HRXCT Facility (Ketcham & Carlson 2001). Table 2 shows the scan parameters used in this study. Because of the wide range of material types and imaging requirements for geological research, data acquisition parameters must typically be customized for any given project. The principal aim of the scans in this study was to be able to discriminate between garnet and the material that makes up inclusion trails within the garnet. A balance was required between the volume of rock scanned to get enough garnets imaged, the spatial resolution of the scans, and the amount of contrast between CT values for the different materials.

Parameter	Value	Parameter	Value
Source Voltage (keV)	150	Voxel size	10.7 x 10.7 x
Beam Current (mA)	0.2	($\mu\text{m} \times \mu\text{m} \times \mu\text{m}$)	13.1
Spot size (μm)	30	Image scale	16-bit
Slice thickness (mm)	0.0131	Views per 360°	1600
Spacing of slices (mm)	0.0131	Time per view (ms)	133
Number of slices	918	Time per slice* (min)	1.3
Scanned height (mm)	12.0	Wedge	SMT**
Field of view (mm)	11.0	Offset	none
Slice resolution (pixels x pixels)	1024 x 1024	Source to Object Distance (mm)	38

* Data for 27 slices acquired simultaneously

** SMT – sodium metatungstate solution mixed to a density of 1.19g/cm^3

Table 2. X-ray CT scan parameters used. See text for discussion.

An X-ray energy of 150 keV was used to provide good material penetration while avoiding beam fluctuations that occasionally occur at higher energies on the UTCT system. The current was set to 0.2 mA, resulting in a focal spot size of roughly 35 μm ; the corresponding loss in sharpness was more than offset in this case by the increase in X-ray intensity and signal to noise ratio. A 1.19 g/cm^3 SMT solution was used for the wedge calibration. A total of 1600 views were acquired per rotation, with a sampling time of 133 ms per view, resulting in a per-rotation time of ~3.5 minutes for data acquisition plus ~0.5 minutes for preliminary data processing. Data for 27 slices were gathered during each rotation, resulting in a per-slice acquisition time of approximately 9 seconds. A total of 918 slices were acquired for each of four cores, and total acquisition time was about 2.5 hours per core. The sinogram data were reconstructed into images on a separate computer after all scan data were acquired, as the acquisition rate outstrips the processing rate. The reconstruction algorithm features re-sampling of the data to a parallel-beam configuration, followed by back-projection using the Laks filter.

2.3 Comparative techniques

A polished thin-section was prepared from the sample analysed by HRXCT in this study. This was done to allow comparison of the images generated with more traditional methods of analysis. Optical microscope images were taken on a Leica DMRXP microscope using a Leica DC300 digital camera. Electron microprobe analyses were made using two machines, a JEOL JX-840 electron probe microanalyser and a JEOL JX-8200 Superprobe. Back-scattered electron (BSE) images and point analyses were made on the JX-840 and X-ray compositional maps were made on the Superprobe. Qualitative point analyses were done using the energy dispersive technique with an accelerating voltage of 15kV, a beam current of 10nA and a count time of 40s on the JX-8200. Fe, Ca, Mg, Mn were mapped using the wavelength dispersive technique with other elements collected simultaneously using the energy dispersive technique. Mapping conditions were an accelerating voltage of 15kV, beam current of 100nA, spot size of 7 μm , step size of 7 μm and count time of 180mS.

2.4 Data analysis

All image analysis and processing was carried out on either James Cook University's high performance computer, Hydra, which is an SGI Origin 3800 with 84 processors, 42 Gigabytes of RAM and 1.5 Terabytes of storage or a Sunblade 2000 with dual processors and 4 Gigabytes of RAM. The images generated by the UT HRXCT facility are 1024 x 1024 pixel, 16-bit images written in a modified tiff format, with one image for each slice. One of the main challenges in working with data derived from X-ray CT is its size, with the volume of data collected for a 12mm length of core in this study being over 1.8 Gb. It is for this reason that a high performance computer was used to analyse the data. Currently available high-end desktop

computers with a large amount of RAM would be sufficient for working with subsets or down sampled versions of the data.

Three-dimensional rendering and slicing were performed using OpenDX (DX), an open source data visualisation program based on IBM, Inc.'s Data Explorer. DX is freely available on the Internet at <http://www.opendx.org/>. ImageMagick, an open source image-handling program available at <http://www.imagemagick.org/>, was used to prepare the data for importing into DX. The tiff files were converted into raw greyscale images that were concatenated into a single file that was then imported into DX and saved in native DX format as positions dependent data. Two versions of the data were imported into DX, one leaving the data intact, the other down sampling the images to 8-bit data at a resolution of 256 x 256 pixels using every third slice. Before down sampling, the image values were rescaled to spread the data over the full 8-bit range. ImageMagick uses the Lanczos sampling algorithm to resample the image by default. The lower resolution version of the data was used for imaging the whole core and locating garnets within the core, with the full resolution data used for detailed analysis of individual porphyroblasts.

The location of the centers of the garnet porphyroblasts was measured using the low-resolution dataset. A subset was then made of the full resolution dataset centered on each porphyroblast with a maximum dimension slightly greater than the maximum dimension of that garnet. This was done to allow the features of individual porphyroblast to be studied in detail and reduce processing time. To visualize inclusion trails in three-dimensions, the matrix material outside the garnets had to be removed (actually assigned a dummy value) because it has similar CT values to the inclusions themselves.

Using DX the data can be viewed as a volume rendering, a slice through the data, as contoured isosurfaces in three-dimensions or as contour lines on a slice through the data. Two-dimensional slices can be made at any orientation through any point in the data volume. When visualizing the data using DX, a color map is used to assign colors (or greyscales) to the data. This allows enhancement of the features of interest, such as inclusion trails in garnet. The 16-bit data depth allows high contrast color maps to be assigned over any given data interval. Aside from DX, there are many commercially available software packages that are suitable for analyzing X-ray CT data thanks largely to medical imaging. Amira <http://www.tgs.com/> and IDL (<http://www.rsinc.com/idl>) are used at the UTCT facility.

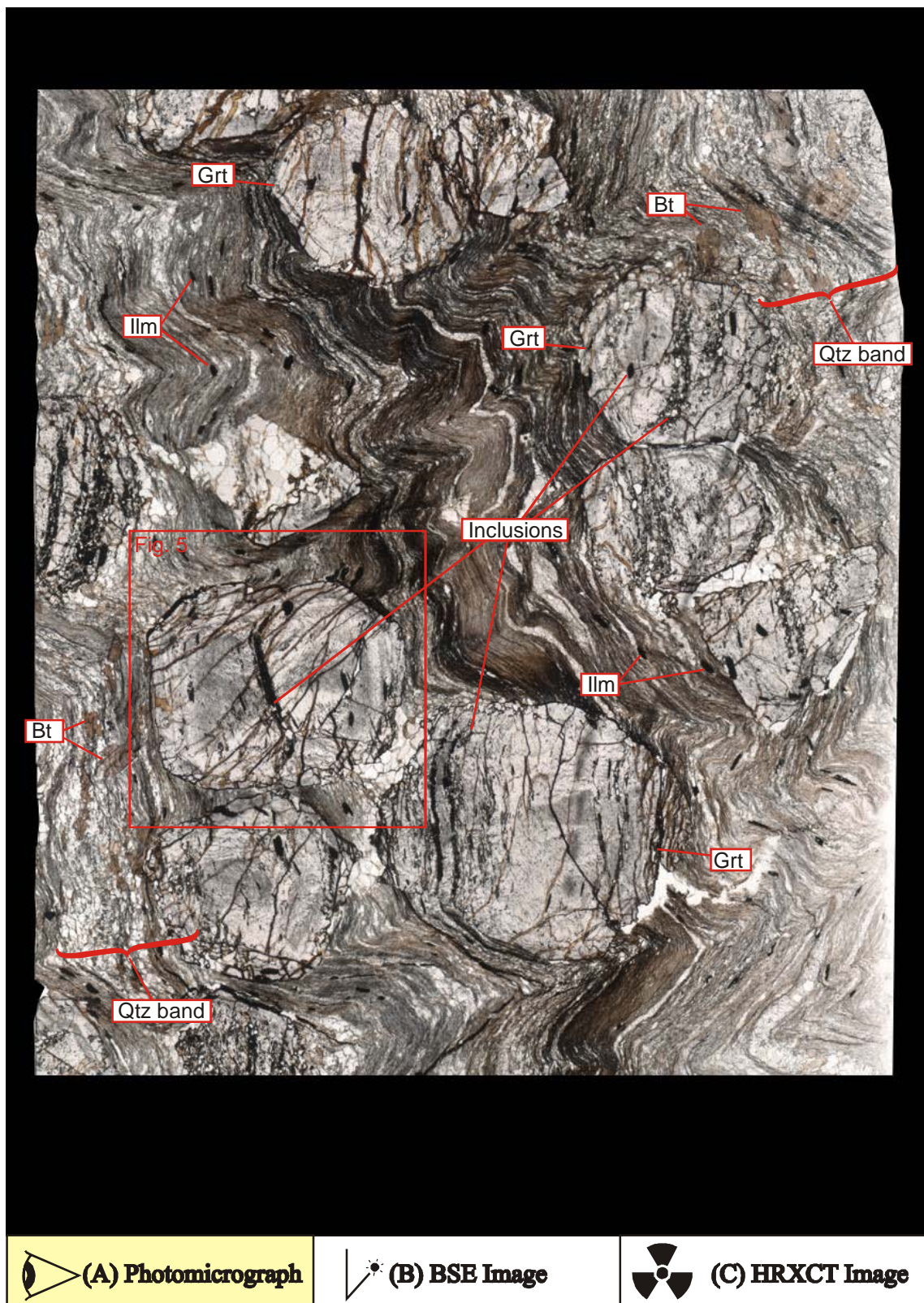


Figure 4. (A) is a photomicrograph of a thin section in plane polarized light through a core analyzed by HRXCT. The section is vertical and oriented west-east, looking north. The images are all of an 11 mm diameter core, 12 mm high, cut parallel to its axis. Mineral name abbreviations are from Kretz (1983). Click on the buttons below the image to select A, B or C. To view this interactive figure, see the interactive Adobe Acrobat document on the CD in appendix A of this thesis.

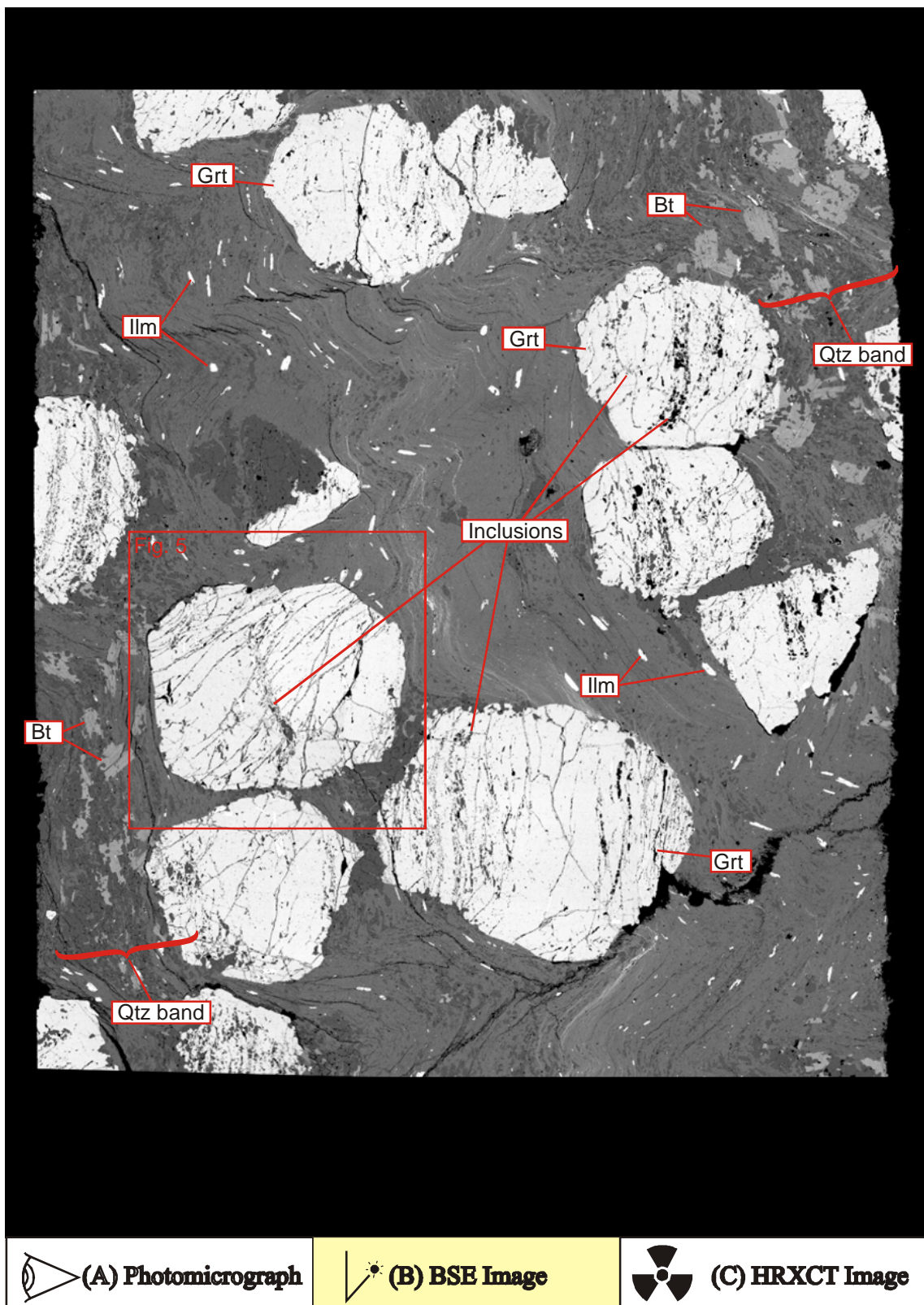


Figure 4 cont... (B) is an electron backscatter image of the thin section shown in (A). The images are all of an 11 mm diameter core, 12 mm high, cut parallel to its axis. Mineral name abbreviations are from Kretz (1983).

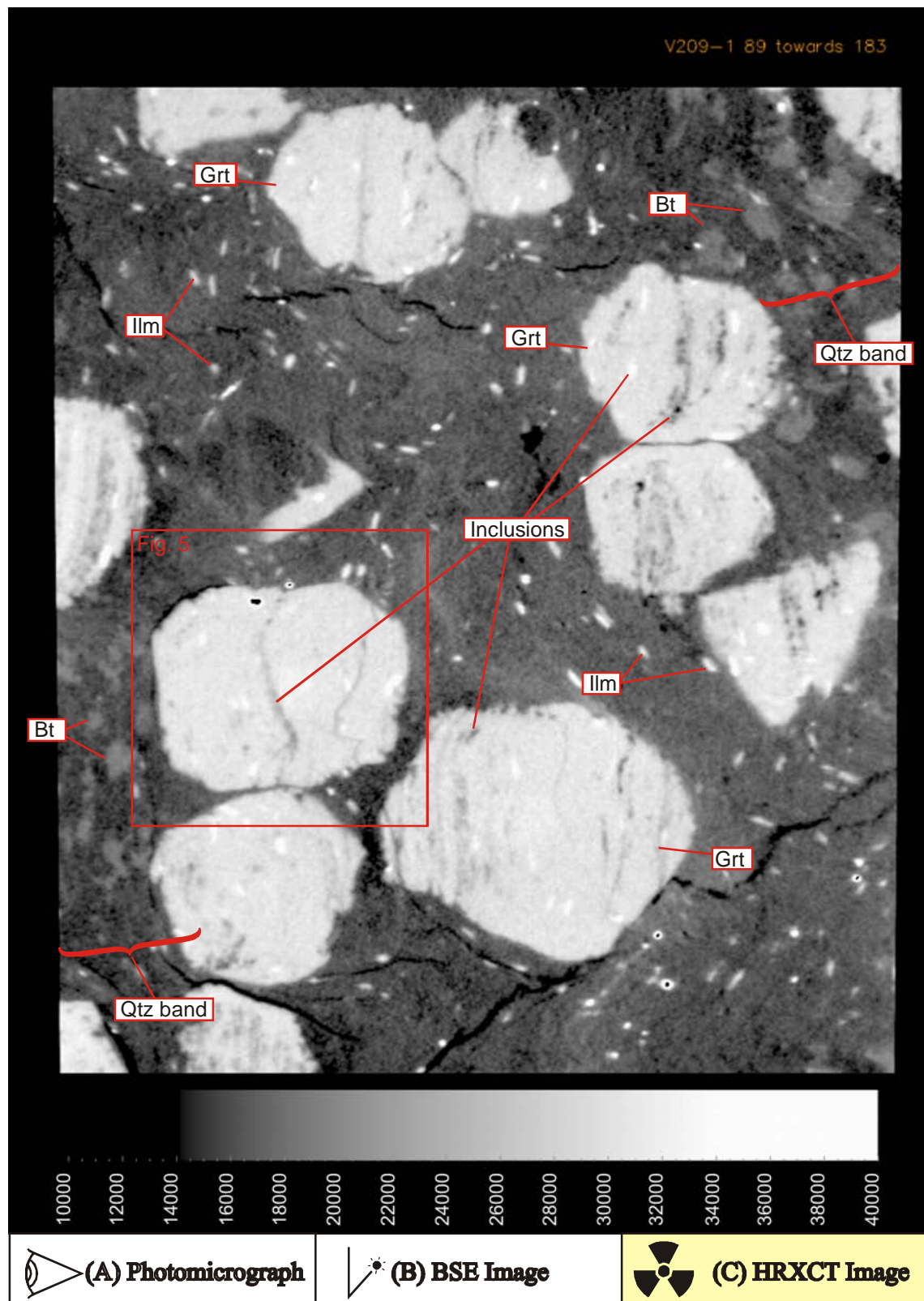


Figure 4 cont... (C) is a slice through the HRXCT data for the core along the plane of the thin section. A gray scale has been applied to the data with lighter levels representing more highly attenuating material. The images are all of an 11 mm diameter core, 12 mm high, cut parallel to its axis. Mineral name abbreviations are from Kretz (1983).

3 Discussion

Figure 4 shows a transmitted light photomicrograph of a thin section made parallel to the axis of a sample core (a), an electron backscatter image of the thin section (b) and a slice through the HRXCT data for that core in the same orientation and position as the thin section (c). This allows comparison between the three techniques. The image produced by HRXCT is similar to that collected by electron backscatter because the two techniques are both imaging similar properties of the sample (the average atomic number). The matrix displays compositional banding at the scale of the thin section with quartz rich bands pitching at 80° to the right in the lower left and upper right corners of the image. This is also apparent in the HRXCT image as darker areas within the matrix, a result of the relatively low attenuation value of quartz (fig. 4c). Biotite porphyroblasts with fine graphitic inclusion trails can also be seen in these parts of the images although the trails are only visible in the photomicrograph. The HRXCT image shows lower resolution for the matrix because of the similarity in attenuation values of quartz and muscovite (fig. 1) and its fine grain size. Fine biotite, which has an attenuation value slightly higher than the other matrix minerals is also present, but partial volume effects due to its fine grain size result in their blending in to the rest of the matrix. Slightly coarser rutile grains are well imaged and provide markers for the matrix foliations. The garnet porphyroblasts stand out clearly in all images, as do their inclusion trails. In this set of figures nothing has been done to enhance any of the features, except to compress the greyscale values for the HRXCT image to a range of 14,000 to 38,000 (instead of 0 to 65,536) to enhance contrast.

Figure 5 shows a series of images of the garnet porphyroblast highlighted in the lower left of figure 4. These include photomicrographs (figs. 5a,b) and compositional maps (figs. 5d-h) as well as a false color HRXCT (fig. 5i) image for comparison. Looking at the photomicrographs a band of hydrated iron oxide with pyrophyllite and quartz can be seen running through the center of the garnet. This band shows clockwise asymmetry with an anti-clockwise flick towards its ends. Fine elongate magnesian siderite grains are also present and show typically high-birefringence in crossed polars (fig. 5b), with iron content similar to garnet, magnesium content higher than garnet (particularly near the centre of the garnet) but no silicon (fig. 5d,e,h). Elongate ilmenite grains are the coarsest inclusions preserved and are generally elongate parallel to the central band. Quartz inclusions (white on the silicon map, fig. 5h) are present as fine grains or clusters that are also elongate. Fine calcium rich inclusions (fig. 5g) are apatite. The porphyroblast has a fine dusting of graphite that is clearly visible in the plane polarized light photomicrograph (fig. 5a) and a weak form of sector zoning is present. At the left and right ends of the porphyroblast, graphite defines more or less vertical bands in the outer 0.2mm of the grain that appear to be continuous with banding in the matrix. This corresponds

with a rim overgrowth and zoning in the magnesium, manganese and calcium composition. A feature that stands out in the photomicrographs is the top-right to bottom-left running iron stained fractures. They appear to have a significant thickness ($\sim 50\mu\text{m}$) but this results from their low angle to the section (east-west, vertical) that has a thickness of approximately $30\mu\text{m}$. The majority of fractures dip at approximately 70° towards 235° and are generally only a few microns thick.

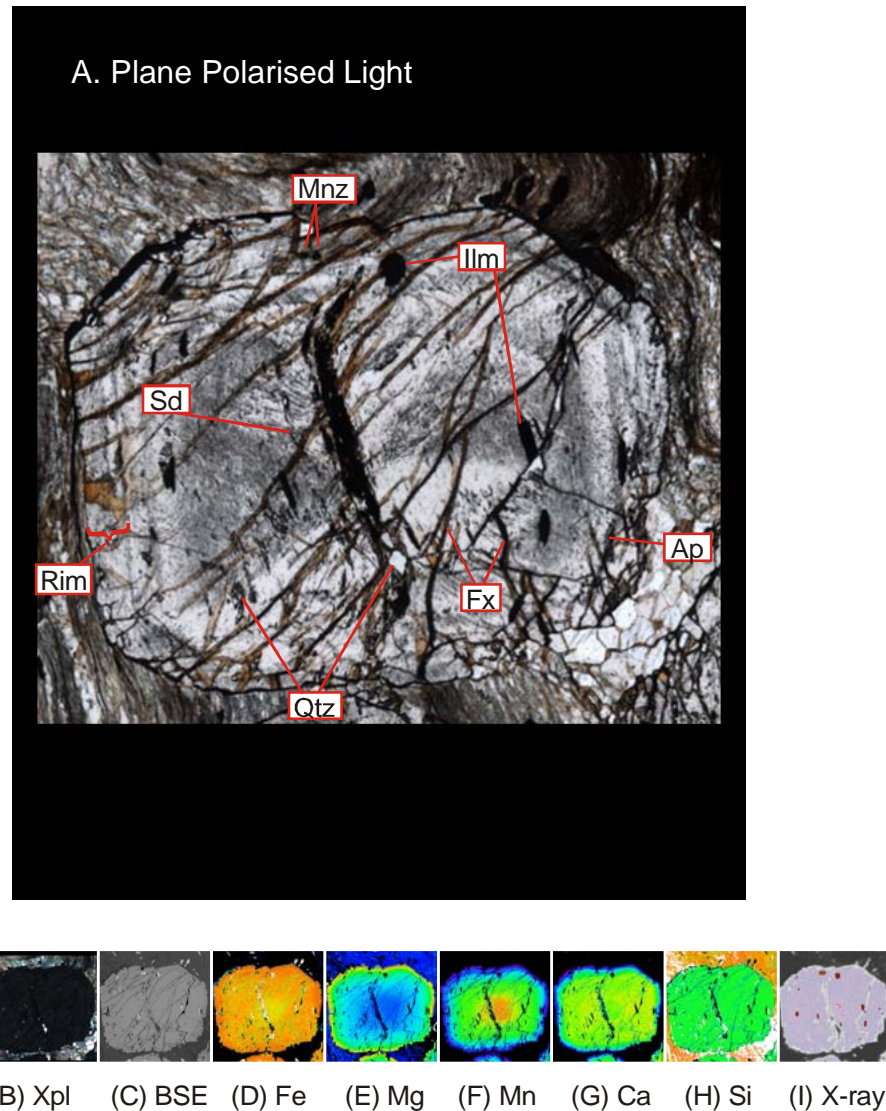


Figure 5. This series of images shows the garnet indicated in figure 4 for detailed examination. (A) and (B) are photomicrographs in plane polarized and crossed polar transmitted light respectively. A BSE image is shown in (C) along with compositional maps for Fe (D), Mg (E), Mn (F), Ca (G), and Si (H). A HRXCT image, which has been assigned a false color scale to highlight features, is shown in (I). All images show a region approximately 3.5mm across. Mineral name abbreviations are from Kretz (1983). Fractures have been labeled Fx. Switch between images by clicking on the thumbnails. See text for further discussion. To view this interactive figure, see the interactive Adobe Acrobat document on the CD in appendix A of this thesis.

The HRXCT image of this porphyroblast (fig 5i) clearly shows the central band and ilmenite grains. In this image a color map has been used to enhance the inclusions, rendering material with CT values lower than garnet shades of grey (hydrated iron oxides, quartz, clay) and material with higher values red-brown (ilmenite). The overall asymmetry of the inclusion trails is clear in this image, including the reversal at the ends of the central band. In this case individual quartz grains in the garnet are generally too fine to image well and only larger grains or accumulations of grains are visible in the HRXCT image. Where these grains or accumulations are elongate they help to define the inclusion trail geometry. Ilmenite grains are generally coarser in this specimen and their elongate nature can be readily seen. Magnesian siderite inclusions cannot be distinguished from garnet because these two phases have very similar attenuation characteristics (fig.1) at the X-ray energies used for this study. The majority of the fractures seen in the photomicrographs (figs. 5a,b) and compositional maps (figs 5d-h) are not visible in the HRXCT image (fig. 5i), because they are generally very fine and not filled by a material with significantly different attenuation characteristics to the garnet. Only coarse fractures are imaged. Similarly, graphite dusting is also too fine and sparse to make an impact on the CT values for the garnet. The two small grains (red spots in figure 5i) at the top of the porphyroblast are monazite, which is very highly attenuating because of its high average atomic weight (they also stand out as two bright spots in the BSE image, fig. 5c). Although these grains are less than 60 μm in diameter, they stand out in the image because they have a much higher attenuation coefficient than the material they are in (fig. 1). The halo-like artifact is a result of smearing in the reconstruction of the image. What appears to be a speckling of ilmenite in the center of the garnet porphyroblast is probably the result of compositional zoning in the garnet. In addition to the major-element zoning shown in Figure 5, qualitative electron microprobe analysis indicates that the core of the garnet is relatively high in yttrium. Estimation of the effects of zoning in both major elements and Y, based on profiles of garnets from the Picuris Mountains by Chernoff and Carlson (1997, 1999), suggest that either may cause a shift in attenuation coefficient on the order of 0.5% with X-rays in the 20-100 keV energy range. This shift is slightly above the lower limit of detectability in CT with a polychromatic X-ray source

This study demonstrates that HRXCT is capable of imaging inclusion trails in garnet porphyroblasts where the inclusions are of suitable size, composition and abundance. The data presented here suggest some guidelines for the selection of the most suitable samples for this technique. Firstly, the spatial resolution of the images is largely controlled by the sample size. The image size is constrained by the number of detectors, in this case 1024, resulting in an image size of 1024 x 1024 for each slice. The smaller the sample, the higher the achievable spatial resolution. Although the theoretical minimum resolution for modern HRXCT systems is around three microns for a sample two to three millimeters in diameter this is really pushing the equipment to its limits. At this scale data acquisition would be more time-intensive (and money-

expensive) in order to obtain relatively noise-free images, as there is much less differential attenuation across small samples. In addition, a smaller focal spot would be required, decreasing X-ray intensity and increasing problems associated with drift in the focal spot position. As a result a study of inclusion trail geometry would ideally involve a sample with five-ten mm diameter garnets that could be scanned individually or in cores drilled from the sample providing a voxel size of five to ten microns. Scanning a larger sample at low resolution would allow the garnets within it to be located for extraction.

The mineralogy, size, density and distribution of inclusions within porphyroblasts dictate which samples are most suitable for the analysis of inclusion trails using CT. Minerals with significantly different attenuation coefficients to garnet provide the best contrast and both quartz and iron/titanium oxides are ideal. It is a happy coincidence that these minerals are the most common inclusions seen in garnet porphyroblasts. Given the voxel size described above, an inclusion size ranging from fifty microns to 0.2 mm in maximum dimension would be ideal, allowing the shape of individual inclusions to be clearly imaged.

An appropriate range for the density of inclusions is from ten to thirty percent. If the density is too high images are confusing, while if it is too low the trails aren't adequately defined. Inclusions that are evenly distributed throughout the porphyroblast provide a clear picture of the overall geometry of the trails. Where they are restricted to bands, either as a relict of primary layering of the rock or as the result of a differentiated crenulation cleavage, they provide marker bands that are continuous through the porphyroblast and allow comparison with geometries predicted from models for the formation of curved inclusion trails (e.g. Stallard et al. 2002, Williams & Jiang 1999). The garnet in figures 5 is a good example of this type of inclusion distribution. The size of the inclusions is less important if they define bands as the bands as a whole would define the inclusion trails.

A powerful advantage of HRXCT is that a true three-dimensional dataset is created and the data can be viewed in a large number of ways. A single porphyroblast can be viewed in three-dimensions, made transparent to highlight the inclusion trails or removed altogether leaving just the inclusions. Intersecting or parallel slices can be made with an infinite range of orientations and through any point in the porphyroblast. Figure 6 demonstrates a range of viewing techniques of the trails from the garnet featured in figure 5. An animation makes the three-dimensional geometry of the trails clearer in figure 7, as does a VRML model that is available for download through appendix 1. These data can also be viewed as stereographic projections allowing the trails to be studied in three-dimensions. Figure 8 is a stereo pair that can be printed to hard copy and viewed using a standard stereo viewer.

Figures 6a-d and 7 are looking south and the asymmetry of the inclusion trails can be clearly seen in three-dimensions. The central band shows a central section that is approximately vertical, with a subtle doubly curving non-cylindrical geometry. Towards the top and bottom

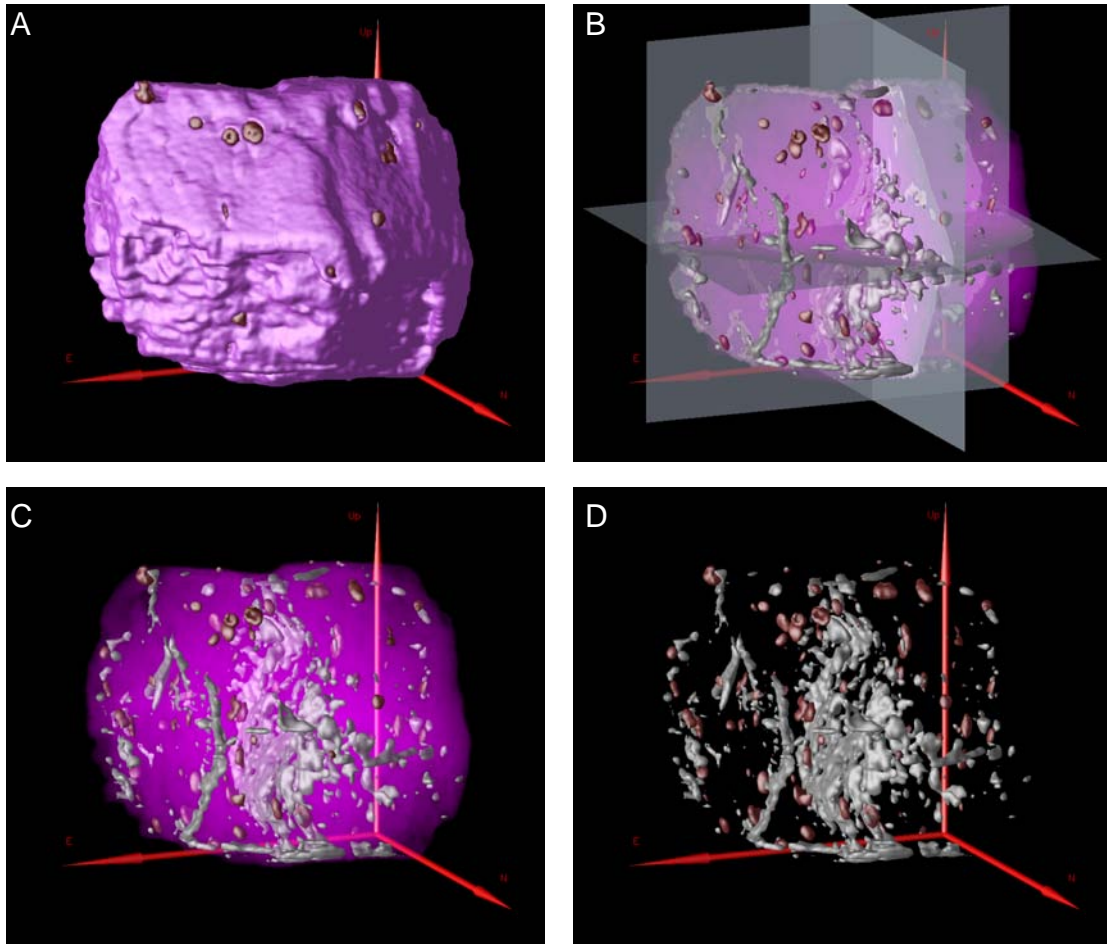


Figure 6. This figure shows different ways of viewing the HRXCT data. All images show the garnet in figure 5, with a field of view of 4.5 cm. (A) shows the garnet rendered as a solid, opaque object. (B) shows the garnet rendered as a transparent object, with the inclusions rendered solid (gray for low attenuation, red-brown for high attenuation), with sections cut horizontally, east-west vertical and north-south vertical. The same image without the sections is shown in (C) and without the sections or garnet in (D).

edges of this band the curvature tightens with the same anti-clockwise, or top to the east, asymmetry. The axis about which this curvature occurs plunges at 2.5° towards 187.5° . This was measured to a 5° interval using a similar technique to that used to measure FIAs in thin section, making many slices through the garnet. This proved to be more reliable than attempting to fit an axis to the three-dimensional data because of the irregular distribution of inclusions. The geometry seen here is referred to as being sigmoidal (as opposed to spiral) and represents approximately 75° of curvature. The flick back at the end of the trails seen in the photomicrographs in figure 5 is also apparent. The axis about which this flick occurs has a trend of 122.5° . It was not possible to accurately measure its plunge of because it occurs over too small a region. As mentioned earlier, fine graphite dusting cannot be imaged by HRXCT so the orientation of trails in the very rim of the garnet could not be measured.

When studying the VRML model in appendix 1 a sub-vertical axis of curvature is also apparent with a south to the east asymmetry. See the Applications section below for a discussion of the measurement of FIAs. It is interesting to note that the ilmenite grains range in shape from fat discs to short rods, all plunging steeply and parallel to the central band. This probably represents the stretching lineation for the foliation defined by the central band.

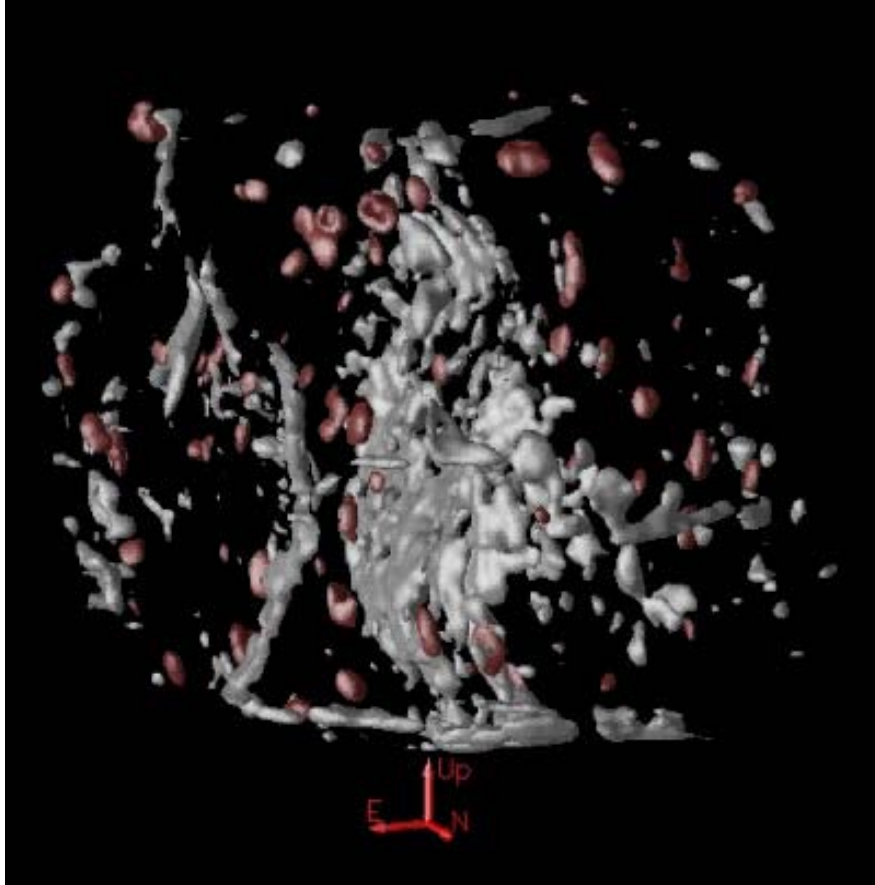


Figure 7. This is an animation that shows the inclusion trails from the garnet featured in figure 5 and 6a-d being rotated through a 40° range about a vertical axis. This allows the three-dimensional geometry of the inclusion trails to be seen more clearly. Note the doubly curving non-cylindrical geometry shown by the central band, which curves about a sub-horizontal, north-south trending axis. A fracture crosses the northeast part of the garnet and is distinguishable from the inclusion trails by its irregular nature and discordance with the rest of the trails. The field of view is approximately 4.5 cm. The animation can be paused and stepped through frame by frame if desired. To view this animation, see the interactive Adobe Acrobat document on the CD in appendix A of this thesis.

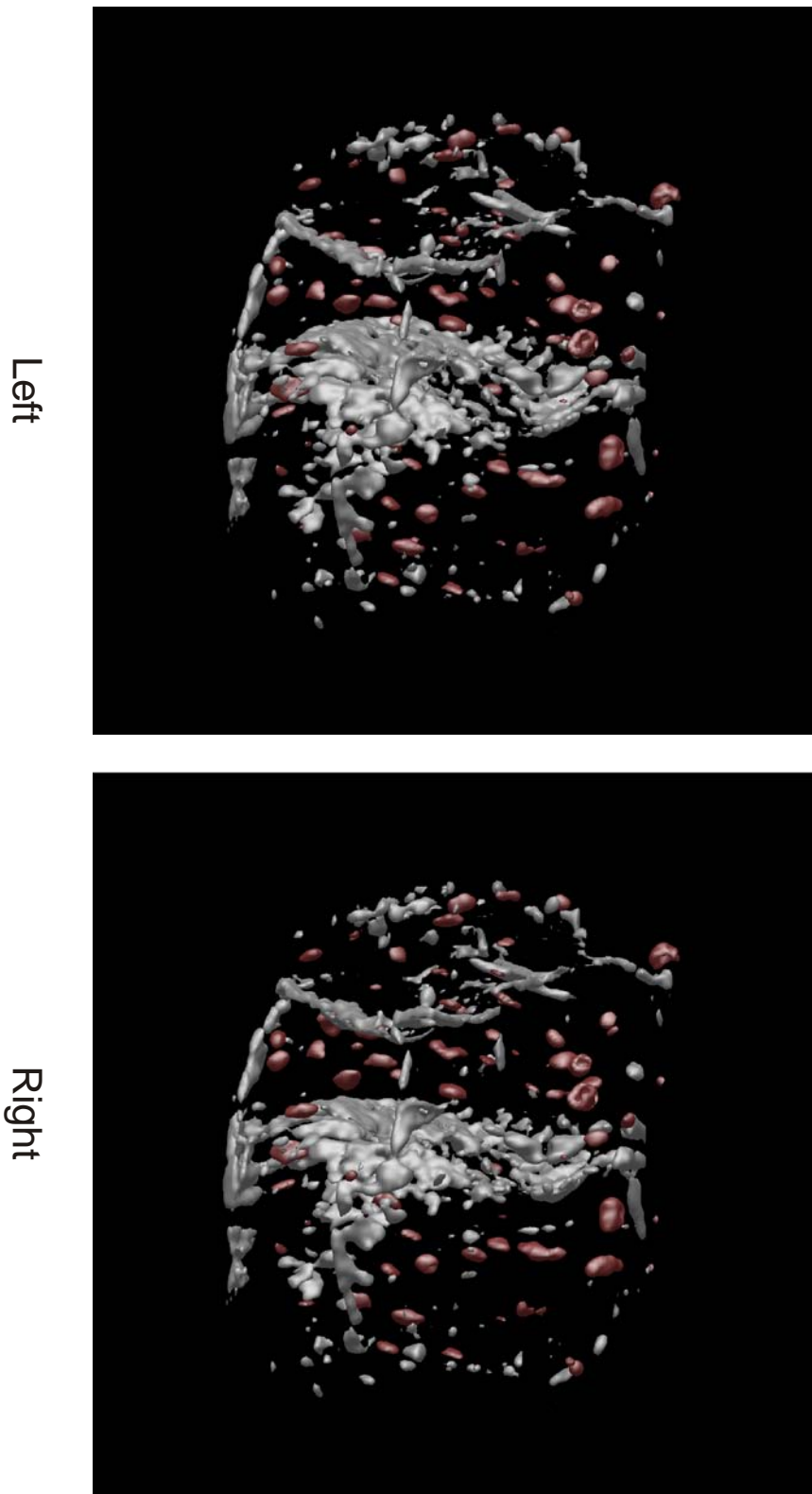


Figure 8. A stereo pair of the three-dimensional image of the inclusion trails in the garnet in figures 5, 6 and 7. This allows the true three-dimensional geometry of these microstructures to be viewed using a standard stereo viewer. Images have a resolution of 375dpi and can be printed in color or greyscale. The field of view is approximately 4.5 cm To print these images, see the interactive Adobe Acrobat document on the CD in appendix A of this thesis.

3.1 Applications

3.1.1 Investigating the three-dimensional geometry of inclusion trails

The most obvious application of this technique is in attempting to answer the question of whether or not curved inclusion trails form as the result of the porphyroblast rotating relative to fixed geographic reference frame or by the overgrowth of a series of foliations. This technique allows detailed three-dimensional study of inclusion trails enabling their geometry to be compared with those predicted from models. Williams and Jiang (1999) provide a criterion with which that the three-dimensional geometry of spiral inclusion trails (as opposed to the two-dimensional geometry) can be used to determine whether rotational or non-rotational models apply. Conversely, Stallard et al (2002) predict that the different processes hypothesized for the formation of inclusion trails may not produce inclusion trail geometries that are significantly different. Unfortunately, the garnets imaged in this study do not contain spirals so no conclusions can be drawn here. However, the data here demonstrate how HRXCT data could be used. The inclusion pattern in figure 9a is similar to the closed loop structures predicted by Stallard et al (fig. 4, 2002), for instance, which they predict will be a feature regardless of how the curved trails form. This geometry is the result of the subtle doubly curving geometry of the trails that demonstrate that if the non-rotation model is correct then the crenulation hinges they grow in are non-cylindrical. This is an example of how HRXCT data can be sectioned at any orientation and the geometry in the section compared with that predicted by a model.

Most of the literature on numerical simulations or theoretical models of inclusion trail development in porphyroblasts are concerned with spiral shaped trails (e.g. Samanta et al. 2002b, Stallard et al. 2002, Williams & Jiang 1999). In reality, sigmoidal trails, as in the data presented here, are much more common than spiral trails. Sigmoidal trails have a simple S or Z shape and a maximum of 90° to 120° of apparent rotation. It is interesting to note that close to the axis of curvature these sigmoidal trails looked like a 180° spiral (figure 9b). This observation reinforces the idea that if three-dimensional data such as presented here are not available then multiple thin sections of differing orientations are needed to see the full complexity of structures preserved in inclusion trails (Cihan 2004). To compare models against reality a selection of samples with inclusion trails that range from true spiral shapes to simple sigmoids is needed. At present, there are only two publications on the three-dimensional geometry of real inclusion trails, one on spirals (Johnson 1993b) and one on millipede structures (Johnson & Moore 1996) and these data need to be added to if our understanding is to be advanced. Aspects of deformation mechanisms themselves revealed from this type of study may be supportive of one model or the other. A key concept of the argument for non-rotation of porphyroblasts is that of deformation partitioning (see Bell 1985) while most rotational arguments are based on simple and pure shear (e.g. Samanta et al. 2002b, Stallard et al. 2002).

How features such as truncation surfaces and millipede structures relate to these processes will be better understood once they have been studied in three-dimensions. For instance, figure 9c shows a truncation surface in a garnet imaged by HRXCT. Study of these features in the sample revealed them to be sub-planar features that curve only slightly around the core of the garnet. The near vertical trails in the core of the garnet curve into these truncation surfaces with an apparent rotation of 90° . This geometry supports the hypothesis that truncations in porphyroblasts are evidence for episodic deformation and metamorphism (Bell et al. 1992c). A full discussion of the three-dimensional geometry of inclusion trails with respect to models for their formation warrants a paper of its own and will not be pursued further here.

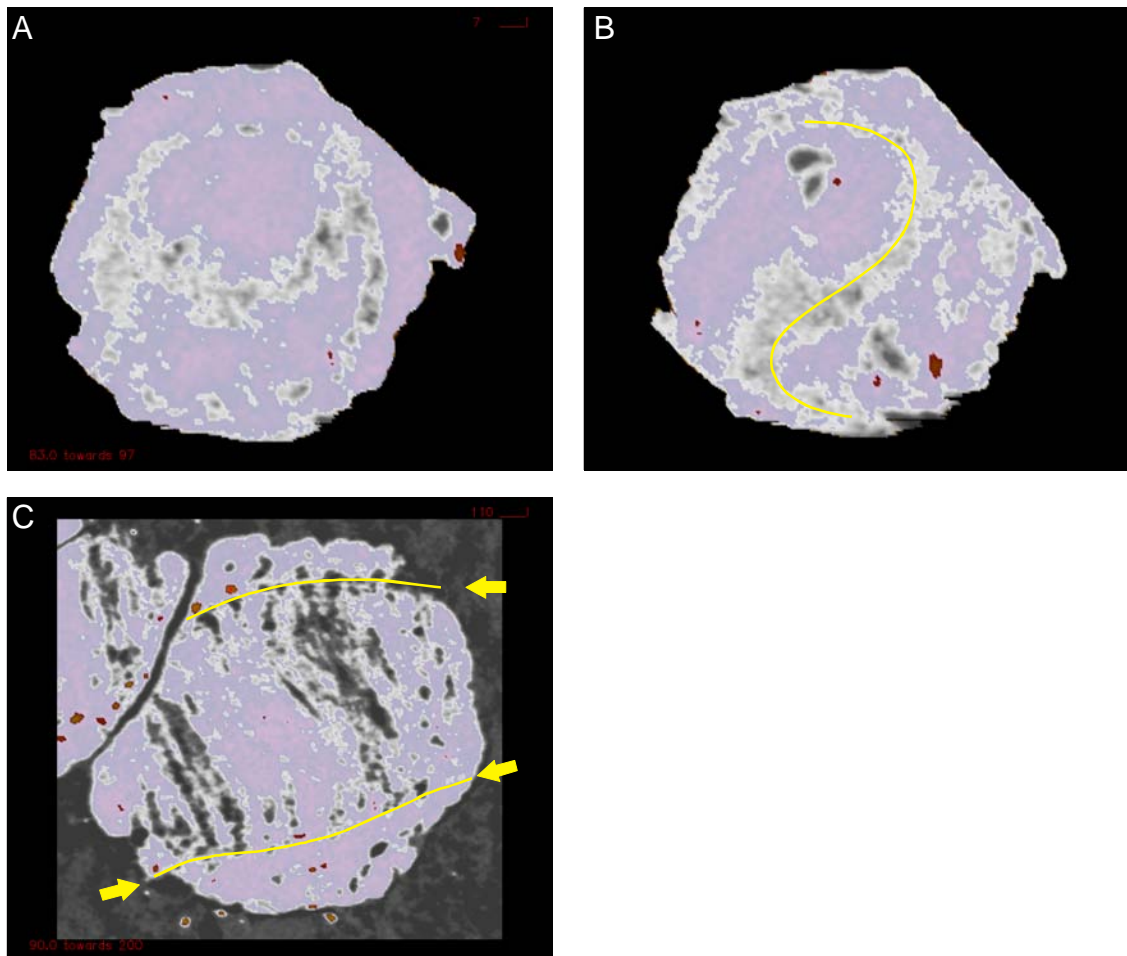


Figure 9. (A) is a section through the garnet in figures 5 through 8 parallel to the axis of curvature showing closed loop structures predicted by Stallard et al (2002). (B) shows a section through the same garnet oriented slightly oblique to the axis of curvature. The apparent 180° spiral geometry (mouse over to highlight) could give a false sense of the amount of curvature if seen only in thin section. A flat truncation (yellow arrows, mouse over to highlight) of a steep foliation with clockwise asymmetry is shown in (C). Field of view 5.5cm. To view this interactive figure, see the interactive Adobe Acrobat document on the CD in appendix A of this thesis.

3.1.2 Assessing the distribution of FIA in a single sample

A concept that has had recent exposure in the literature is that of the FIA (foliation intersection/inflection axis preserved in porphyroblasts), which measures the axis of curvature of curved inclusion trails (Bell et al. 1995, Bell et al. 1998, Hayward 1990). In a review of the uses of porphyroblast microstructures, Johnson (1999) raised some important questions regarding FIA, mostly regarding the spread of orientations obtained for a single sample and the error therein. The main problem in addressing these questions is that the technique for determining FIA only allows the trend to be determined for a sample, rather than for individual porphyroblasts. As a result, it is impossible to know what their porphyroblast to porphyroblast variation is and following on from this, what the true statistical spread of trends for a sample is. To allow FIA to be used to their full potential, questions about the statistical confidence that can be assigned to determined trends need to be addressed.

The HRXCT technique provides a method for measuring the FIA of individual porphyroblasts, thus allowing the range of their orientations to be determined. This is the subject of the study for which the data presented here were collected and a paper discussing the results is in preparation. Two FIA could be measured in this sample. The first is for the broad central or core part of the trail, which was measured in 58 garnets and has a mean orientation plunging at 10.6° towards 200.7° . The data are symmetrical and forms a clustered distribution (figure 10b) with a 95% confidence cone semi-angle of 4.1° . The second is in the median part of the garnet (the flick back in figure 5) for which only the trend could be measured reliably. It was measured in 17 porphyroblasts and a mean value of 116.9° was obtained, with a 95% confidence interval of $\pm 2.7^\circ$ (figure 10c). The sub-planar part of the trails was also measured in 55 of the garnets for which core FIA were measured (the other three either had too few inclusions in the central part or were too smoothly curved) and while they are more dispersed than the FIA data they have a similar distribution pattern with a mean orientation plunging at 18.0° towards 292.8° (figure 10a). There is a strong correlation between the trend of the core foliation and core FIA. There is no evidence in the data to suggest that the event that formed the median FIA in anyway modified (i.e. rotated) the distribution of structures already preserved in the cores of the garnet. This observation, along with the clustered nature of the FIA data from the core of the garnets, suggests that the porphyroblasts in this sample have not rotated. The non-rotation interpretation of the history preserved here is that a steep foliation trending 30° - 210° is overprinted by a flat lying crenulation cleavage. The garnet nucleates and grows during this event and preserves the curvature of the steep foliation into the flat. The core FIA orientation is that of the intersection between the earlier steep and following flat foliation. Another steep 115° - 295° trending foliation then forms and is overgrown by a small radial increment that forms the median part of the garnet. A final increment of growth forms the rim of the garnet, most likely in a flat foliation. The steep FIA seen in the VRML model (appendix 1)

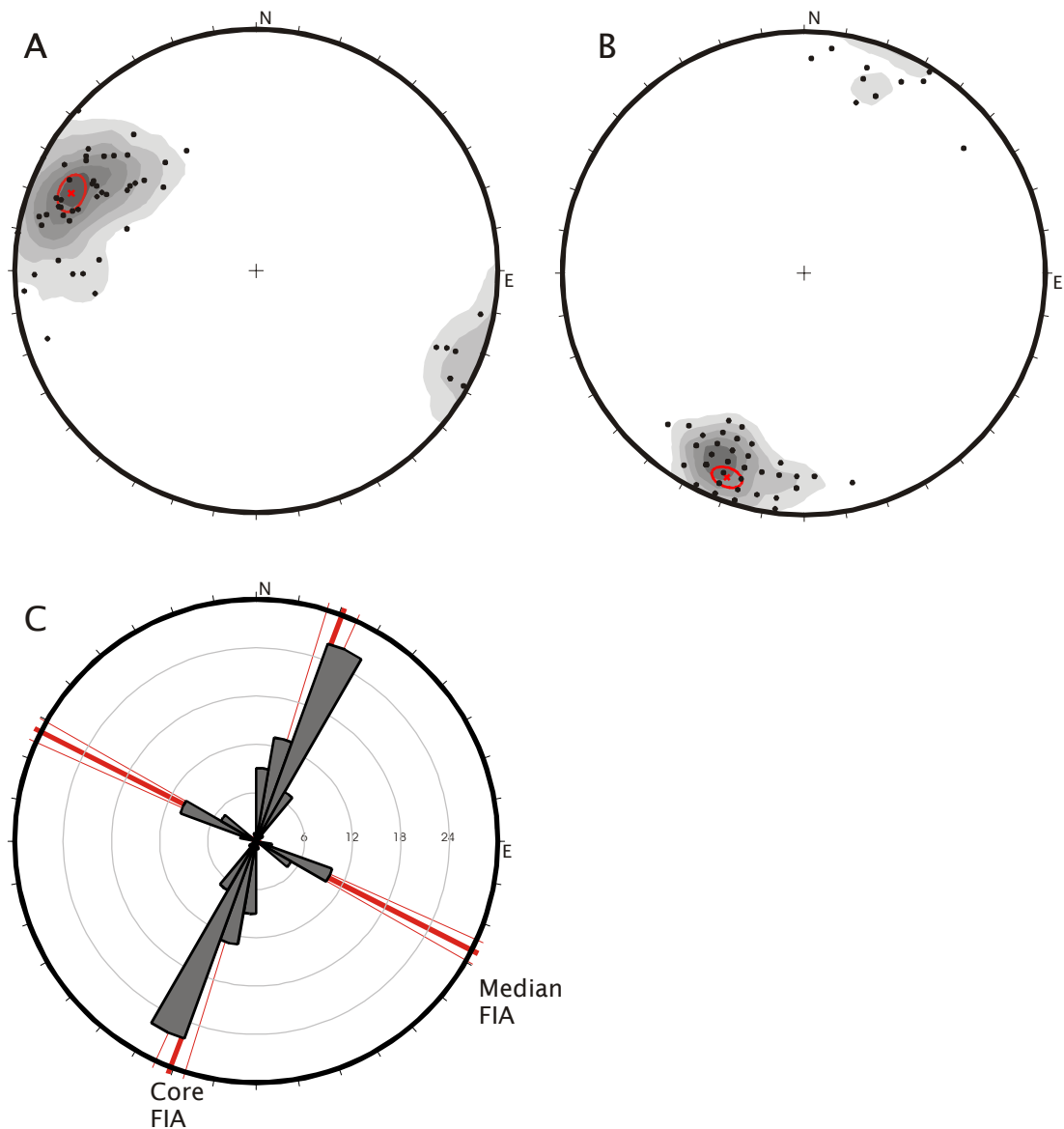


Figure 10. This figure shows preliminary data from a study of the distribution of FIA in individual porphyroblasts from a single sample. (A) and (B) are equal area stereo nets showing the orientations of inclusion trails measured in the cores of 55 garnets (plotted as poles) and the orientations of FIA from the core of 58 garnets respectively. These data are plotted as points and density contours as the FIA data have some repeat readings. The mean orientations are marked with a red cross and the 95% confidence cone as a red circle. The regular spacing in the core FIA data is a result of them being measured in 5° intervals. (C) is a rose diagram showing the FIA data from the garnet cores and an additional 17 measurements from their medians. See text for further discussion.

is most likely the result of the intersection between relicts of the original steep foliation (that has been protected from the effects of the flat foliation in the strain shadow immediately adjacent the garnet) and the later steep foliation that formed the median FIA.

Previously, three-dimensional datasets have been created by indirect construction from a series of two-dimensional thin-sections through a porphyroblast (e.g. Johnson 1993b, Johnson & Moore 1996) or serial lapping (e.g. Daniel & Spear 1998, Daniel & Spear 1999,

Marschallinger 1998, Spear & Yao 2001, Spear & Daniel 1998, Spear & Daniel 2001). These methods are time consuming – to achieve a similar resolution of data to that gathered by HRXCT in this study, Marschallinger's (1998) technique would require 300 cycles of lapping and image collection for a 3mm diameter garnet. The HRXCT data presented here, representing approximately four cubic centimeters of rock, was gathered in about a day and a half. There are two advantages of serial lapping over HRXCT. Firstly, the resolution in the two-dimensional slices being mapped can be significantly higher. Secondly, a range of images can be collected for each slice, such as optical photographs, back-scattered electron images, secondary electron images and compositional maps, providing compositional data in three-dimensions. However, for textural analysis on a truly three-dimensional basis, HRXCT is an invaluable tool. Furthermore, these approaches are not exclusive of each other: because HRXCT is non-destructive, the samples are preserved for future compositional analysis, which can be targeted at the most potentially informative porphyroblasts.

3.2 Future Directions in HRXCT

While this technique is readily available now and provides an excellent tool for the study of geological textures, it continues to be refined. Research into improved reconstruction algorithms that reduce artifacts or improve processing time continues (e.g. De Man et al. 2001, Elbakri & Fessler 2003, Kalukin et al. 2000, Yamaya et al. 2000). This, along with the steady increase in computing power and advances in detector technology, will allow ultra-high resolution studies with improved differentiation of materials. The currently available X-ray CT technology is limited by the use of polychromatic X-ray sources. This means that the X-ray attenuation coefficients can not be determined quantitatively. Tsuchiyama et al. (2002) described a technique for quantifying the relationship between CT values and linear attenuation coefficients by normalizing the CT values to a known standard. Another possibility is the use of monochromatic X-ray sources which allow quantitative determination of the X-ray coefficients of the material being scanned (e.g. Bonse & Busch 1996). This can only be done with synchrotron radiation as an X-ray source (Dilmanian 1992, Natterer & Ritman 2002) at this time, which limits its availability. The HRXCT technique described here relies on the absorption of X-rays. The use of synchrotron radiation sources have allowed other methods to be investigated including dual energy subtraction (Torikoshi et al. 2001, Torikoshi et al. 2003), fluorescence (Takeda et al. 2000) and phase shift contrast (Bonse & Beckmann 2001, Bronnikov 2002), all of which are more sensitive to variations in materials than conventional attenuation contrast methods.

In addition, specialized software tools for efficiently making geologically useful measurements in three-dimensional volumes are under continuous development. Examples include measuring the size and shape characteristics of multiple crystals, clasts or vesicles

(Ketcham 2004, Koeberl et al. 2002, Proussevitch et al. 1998) and three-dimensional fabric orientation and strength (Ketcham & Ryan 2004).

4 Conclusions

Computed X-ray tomography continues to find a broader range of application in the geological sciences. Here, its viability as a technique for the imaging of the three-dimensional geometry of inclusion trails in garnet porphyroblasts has been demonstrated. Preliminary studies have given the range of FIA orientations in a single sample for the first time and given support to the non-rotational argument for the formation of curved inclusion trails. With the selection of samples following the guidelines given here, the study of the three-dimensional geometry of curved inclusion trails in garnet can be furthered. This will help to address the ongoing controversy of the mode of formation of these features. The FIA concept can be tested further allowing their significance to be better understood.

References

- Aerden, D. G. A. M. 1995. Porphyroblast non-rotation during crustal extension in the Variscan Lys-Caillaouas Massif, Pyrenees. *Journal of Structural Geology* **17**, 709-725.
- Bell, T. H. 1985. Deformation partitioning and porphyroblast rotation in metamorphic rocks: a radical reinterpretation. *Journal of Metamorphic Geology* **3**, 109-118.
- Bell, T. H., Forde, A. & Hayward, N. 1992a. Do smoothly curved, spiral-shaped inclusion trails signify porphyroblast rotation?: Reply. *Geology* **20**(11), 1055-1056.
- Bell, T. H., Forde, A. & Wang, J. 1995. A new indicator of movement direction during orogenesis: measurement technique and application to the Alps. *Terra Nova* **V. 7**, 500-508.
- Bell, T. H., Hickey, K. A. & Upton, G. J. G. 1998. Distinguishing and correlating multiple phases of metamorphism across a multiply deformed region using the axes of spiral, staircase and sigmoidal inclusion trails in garnet. *Journal of Metamorphic Geology* **16**(6), 767-794.
- Bell, T. H., Johnson, S. E., Davis, B., Forde, A., Hayward, N. & Witkins, C. 1992b. Porphyroblast inclusion-trail orientation data; eppure non son girate! *Journal of Metamorphic Geology* **10**(3), 295-307.
- Berger, M. J., Hubbell, J. H., Seltzer, S. M., Coursey, J. S. & Zucker, D. S. 1999. XCOM: Photon Cross Section Database (version 1.2), [Online]. **2002**. National Institute of Standards and Technology, Gaithersburg, MD.
- Bonse, U. & Beckmann, F. 2001. Multiple-beam X-ray interferometry for phase-contrast microtomography. *Journal of Synchrotron Radiation* **8**(Part 1), 1-5.
- Bonse, U. & Busch, F. 1996. X-ray computed microtomography (μ CT) using synchrotron radiation (SR). *Progress in biophysics and molecular biology* **65**, 133-169.
- Bronnikov, A. V. 2002. Theory of quantitative phase-contrast computed tomography. *Journal of the Optical Society of America A-Optics & Image Science* **19**(3), 472-480.
- Carlson, W. D. & Denison, C. 1992. Mechanisms of porphyroblast crystallization; results from high-resolution computed X-ray tomography. *Science* **257**(5074), 1236-1239.
- Chernoff, C. B. & Carlson, W. 1997. Disequilibrium for Ca during growth of pelitic garnet. *Journal of Metamorphic Geology* **15**(4), 421-438.
- Chernoff, C. B. & Carlson, W. 1999. Trace element zoning as a record of chemical disequilibrium during garnet growth. *Geology* **27**(6), 555-558.

- Cifelli, R. L., Rowe, T. B., Luckett, W. P., Banta, J., Reyes, R. & Howes, H. I. 1996. Fossil evidence for the origin of the marsupial pattern of tooth replacement. *Nature* **379**, 715-718.
- Cihan, M. 2004. The drawbacks of sectioning rocks relative to fabric orientations in the matrix: A case study from the Robertson River Metamorphics (Northern Queensland, Australia). *Journal of Structural Geology* **26**, 2157-2174.
- Daniel, C. G. & Spear, F. S. 1998. Three-dimensional patterns of garnet nucleation and growth. *Geology* **v.26**, 503-506.
- Daniel, C. G. & Spear, F. S. 1999. The clustered nucleation and growth processes of garnet in regional metamorphic rocks from north-west Connecticut, USA. *Journal of Metamorphic Geology* **17**(5), 503.
- De Man, B., Nuyts, J., Dupont, P., Marchal, G. & Suetens, P. 2001. An iterative maximum-likelihood polychromatic algorithm for CT. *IEEE Transactions on Medical Imaging* **20**(10), 999-1008.
- Denison, C., Carlson, W. D. & Ketcham, R. A. 1997. Three-dimensional quantitative textural analysis of metamorphic rocks using high-resolution computed X-ray tomography: Part I. Methods and techniques. *Journal of Metamorphic Geology* **15**(1), 29-44.
- Dilmanian, F. A. 1992. Computed tomography with monochromatic X-rays. *American Journal of Physiological Imaging* **7**, 175-193.
- Elbakri, I. A. & Fessler, J. A. 2003. Segmentation-free statistical image reconstruction for polyenergetic x-ray computed tomography with experimental validation. *Physics in Medicine & Biology* **48**(15), 2453-2477.
- Hayward, N. 1990. Determination of early fold axis orientations in multiply deformed rocks using porphyroblast inclusion trails. *Tectonophysics* **V. 179**, 353-369.
- Ikeda, T., Shimobayashi, N., Wallis, S. R. & Tsuchiyama, A. 2002. Crystallographic orientation, chemical composition and three dimensional geometry of sigmoidal garnet: evidence for rotation. *Journal of Structural Geology* **24**, 1633-1646.
- Johnson, S. E. 1993. Unravelling the spirals: a serial thin-section study and three dimensional computer-aided reconstruction of spiral-shaped inclusion trails in garnet porphyroblasts. *Journal of Metamorphic Geology* **11**, 621-634.
- Johnson, S. E. 1999. Porphyroblast microstructures: A review of current and future trends. *American Mineralogist* **V.84**, 1711-1726.
- Johnson, S. E. & Moore, R. R. 1996. De-bugging the 'millipede' porphyroblast microstructure: a serial thin-section study and 3-D computer animation. *Journal of Metamorphic Geology* **14**, 3-14.
- Jones, K. W., Feng, H., Lindquist, W. B., Adler, P. M., Thovert, J. F., Vekemans, B., Vincze, L., Szaloki, I., Van Grieken, R., Adams, F. & Riekel, C. 2003. Study of the microgeometry of porous materials using synchrotron computed microtomography. In: *Applications of X-Ray Computed Tomography in the Geosciences* (edited by Mees, F., Swennen, R., Van Geet, M. & Jacobs, P.). *Geological Society Special Publication (215)* **215**. Geological Society of London, London, 39-49.
- Kak, A. C. & Slaney, M. 1988. *Principles of Computerized Tomographic Imaging*. The Institute of Electrical and Electronics Engineers, Inc., New York.
- Kalukin, A. R., Van Geet, M. & Swennen, R. 2000. Principal components analysis of multienergy X-ray computed tomography of mineral samples. *IEEE Transactions on Nuclear Science* **47**(5), 1729-1736.
- Ketcham, R. A. 2004. Efficient and flexible three-dimensional measurement of features in CT data volumes: implications for quantitative analysis of metamorphic textures. In: *32nd International Geological Congress Abstract Volume, Part 1*, Florence, Italy, Abstract 93-4, 445.
- Ketcham, R. A. & Carlson, W. D. 2001. Acquisition, optimization and interpretation of X-ray computed tomographic imagery: applications to the geosciences. *Computers and Geosciences* **27**, 381-400.
- Ketcham, R. A. & Ryan, T. 2004. Quantification and visualization of anisotropy in trabecular bone. *Journal of Microscopy* **213**, 158-171.

- Koeberl, C., Denison, C., Ketcham, R. A. & Reimold, W. U. 2002. High resolution X-ray computed tomography of impactites. *Journal of Geophysical Research - Planets* **107(E10)**, 5089.
- Krukowski, S. T. 1988. Sodium metatungstate: a new heavy-mineral separation medium for the extraction of conodonts from insoluble residues. *Journal of Paleontology* **62(2)**, 314-316.
- Kyle, J. R. & Ketcham, R. A. 2003. In-situ distribution of gold in ores using high-resolution X-ray computed tomography. *Economic Geology* **98**, 1697-1701.
- Marschallinger, R. 1998. Three-dimensional reconstruction and modelling of microstructures and microchemistry in geological materials. *Scanning* **20**, 65-73.
- Masuda, T. & Mochizuki, S. 1989. Development of snowball structure: numerical simulation of inclusion trails during synkinematic porphyroblast growth in metamorphic rocks. *Tectonophysics* **170**, 141-150.
- Mees, F., Swennen, R., van Geet, M. & Jacobs, P. 2003. *Applications of X-ray computed tomography in the geosciences*. Geological Society of London, London.
- Natterer, F. & Ritman, E. L. 2002. Past and Future Directions in X-Ray Computed Tomography (CT). *International Journal of Imaging Systems and Technology* **12**, 175-187.
- Passchier, C. W., Trouw, R. A. J., Zwart, H. J. & Vissers, R. L. M. 1992. Porphyroblast rotation: eppur si muove? *Journal of Metamorphic Geology* **10**, 283-294.
- Powell, D. & Treagus, J. E. 1967. On the geometry of S-shaped inclusion trails in garnet porphyroblasts. *Mineralogical Magazine* **36**, 453-456.
- Powell, D. & Treagus, J. E. 1970. Rotational fabrics in metamorphic minerals. *Mineralogical Magazine* **37**(No. 291), 801-813.
- Proussevitch, A., Ketcham, R. A., Carlson, W. & Sahagian, D. 1998. Preliminary results of X-ray CT analysis of Hawaiian vesicular basalts. In: *American Geophysical Union 1998 spring meeting* (edited by Anonymous) **79**. American Geophysical Union, 360.
- Ramsay, J. G. 1962. The geometry and mechanics of formation of 'similar' type folds. *Journal of Geology* **70**, 309-327.
- Rosenfeld, J. L. 1970. *Rotated Garnets in Metamorphic Rocks*. Geological Society of America Special Paper, 129. Geological Society of America, Boulder, Colorado.
- Rowe, T. 1996. Coevolution of the mammalian middle ear and neocortex. *Science* **273**, 651-654.
- Samanta, S. K., Mandal, N., Chakraborty, C. & Majumder, K. 2002. Simulation of inclusion trail patterns within rotating synkinematic porphyroblasts. *Computers and Geosciences* **28**, 297-308.
- Schoneveld, C. 1977. A study of some typical inclusion patterns in strongly paracrystalline-rotated garnets. *Tectonophysics* **39**, 453-471.
- Spear, F. & Yao, K. 2001. The three dimensional geometry of garnet growth, Harpswell Neck, Maine, USA. In: *Eleventh Annual V.M. Goldschmidt Conference, Hot Springs, VA, USA. Abstract number, 3693*. (edited by Bodnar, R. J. & Hochella, M. F.). Lunar and Planetary Institute, Houston, Texas.
- Spear, F. S. & Daniel, C. G. 1998. Three-dimensional imaging of garnet porphyroblast sizes and chemical zoning: Nucleation and growth history in the garnet zone. *Geological Materials Research* **1**(1), 1-43.
- Spear, F. S. & Daniel, C. G. 2001. Diffusion control of garnet growth, Harpswell Neck, Maine, USA. *Journal of Metamorphic Geology* **19**(2), 179.
- Stallard, A. & Hickey, K. A. 2001. Shear zone vs folding for spiral inclusion trails in the Canton Schist. *Journal of Structural Geology* **23**, 1845-1864.
- Stallard, A., Ikei, H. & Masuda, T. 2002. Numerical simulations of spiral-shaped inclusion trails: can 3D geometry distinguish between end-member models of spiral formation? *Journal of Metamorphic Geology* **20**, 801-812.
- Takeda, T., Momose, A., Yu, Q. W., Yuasa, T., Dilmanian, F. A., Akatsuka, T. & Itai, Y. 2000. New types of X-ray computed tomography (CT) with synchrotron radiation: Fluorescent X-ray CT and phase-contrast X-ray CT using interferometer. *Cellular & Molecular Biology* **46**(6), 1077-1088.

- Torikoshi, M., Tsunoo, T., Endo, M., Noda, K., Kumada, M., Yamada, S., Soga, F. & Hyodo, K. 2001. Design of synchrotron light source and its beamline dedicated to dual-energy x-ray computed tomography. *Journal of Biomedical Optics* **6**(3), 371-377.
- Torikoshi, M., Tsunoo, T., Sasaki, M., Endo, M., Noda, Y., Ohno, Y., Kohno, T., Hyodo, K., Uesugi, K. & Yagi, N. 2003. Electron density measurement with dual-energy x-ray CT using synchrotron radiation. *Physics in Medicine & Biology* **48**(5), 673-685.
- Tsuchiyama, A., Nakamura, T., Nakano, T. & Nakamura, N. 2002. Three-dimensional description of the Kobe meteorite by micro X-ray CT method: Possibility of three-dimensional curation of meteorite samples. *Geochemical Journal* **36**, 369-390.
- Wellington, S. L. & Vinegar, H. J. 1987. X-ray computerized tomography. *Journal of Petroleum Technology*(August 1987), 885-898.
- Williams, P. F. & Jiang, D. 1999. Rotating garnets. *Journal of Metamorphic Geology* **17**, 367-378.
- Yamaya, T., Obi, T., Yamaguchi, M. & Ohyama, N. 2000. An acceleration algorithm for image reconstruction based on continuous-discrete mapping model. *Optical Review* **7**(2), 132-137.

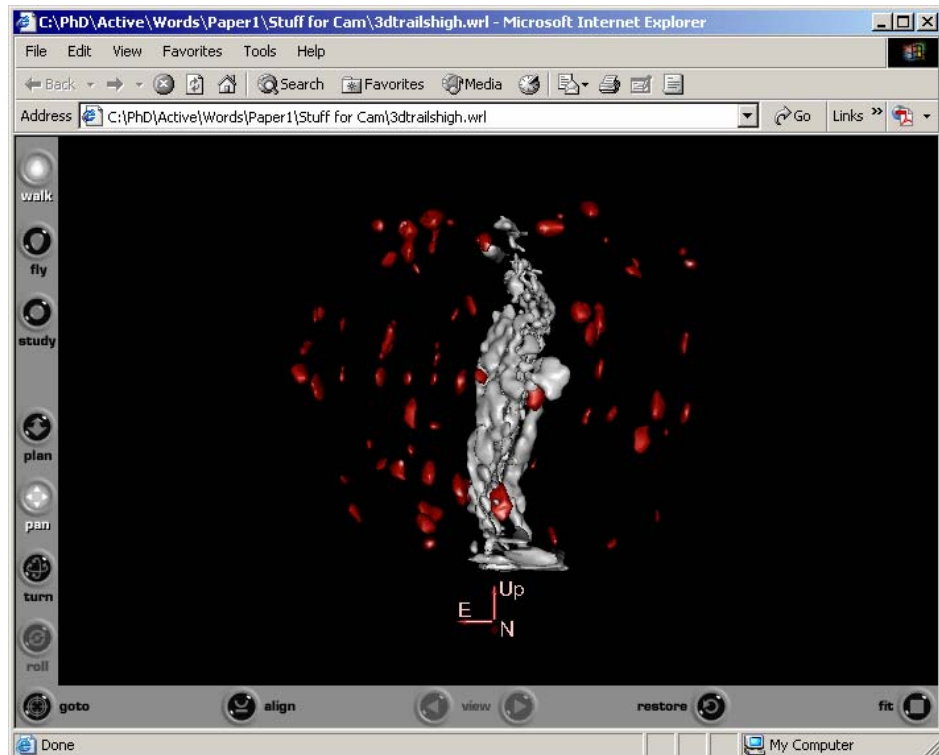
Appendix 1. VRML Files

A vrmf model of the data shown in figure 7 is available on the attached CD in \\chapter1\vrml. There are two versions of this model, a low res version (3.3MB) or a high re version (7.5MB). Some of the inclusions around the edge of the garnet and fractures have been removed from the original dataset to allow the trails to be seen more clearly.

These models are best viewed using the freely available Cortona[®] VRML Client which works as a plug-in for most internet browsers. Cortona is available on the attached CD or at <http://www.parallelgraphics.com/products/cortona/> (Mac users see links on right side of page). Cortona is available for Windows, Mac OS X and Mac OS 9 operating systems.

Viewing VRML files in Cortona VRML Client

To view one of the vrmf files, download it to your local hard drive. Open the web browser for which you have installed the Cortona VRML Client and go to File, Open and browse to the vrmf file and open it. This will launch the Cortona VRML Client within a browser window, which should look something like this



Viewing a scene in Cortona VRML Client is a lot like looking at an object through a camera. You can move (navigate) the camera around so that you can look at different views. There are three different navigation modes available – Walk, Fly and Study. The study mode is recommended for viewing the vrmf models presented here.

Clicking on the *study* and *plan* buttons allows you to zoom in and out by clicking and dragging the mouse up and down and to rotate the object by clicking and dragging to the left or right.

Clicking on the *study* and *pan* buttons lets you pan left, right, up or down by clicking and dragging the mouse in the direction you want to go.